PAPER

# ANCF-based dynamic modeling of variable curvature soft pneumatic actuators with experimental verifications

To cite this article: Yu Rong and Guoying Gu 2024 *Smart Mater. Struct.* **33** 095007

IOP Publishing Smart Materials and Structures
Smart Mater. Struct. **33** (2024) 095007 (12pp) https://doi.org/10.1088/1361-665X/ad63e8

# ANCF-based dynamic modeling of variable curvature soft pneumatic actuators with experimental verifications

**Yu Rong**[1,2] **and Guoying Gu**[1,2,3,*]

[1] Robotics Institute, Shanghai Jiao Tong University, Shanghai 200240, People's Republic of China
[2] State Key Laboratory of Mechanical System and Vibration, Shanghai Jiao Tong University, Shanghai 200240, People's Republic of China
[3] Meta Robotics Institute, Shanghai Jiao Tong University, Shanghai 200240, People's Republic of China

E-mail: guguoying@sjtu.edu.cn

Received 1 June 2024, revised 28 June 2024
Accepted for publication 16 July 2024
Published 2 August 2024

**Abstract**

Accurate and computationally efficient models of soft pneumatic actuators are crucial for utilizing their compliance in various fields. However, existing research primarily relies on the piecewise constant curvature assumption or the quasi-static assumption, only valid in limited situations. In this paper, we present a dynamic model based on absolute nodal coordinate formulation (ANCF) that simultaneously accounts for variable curvature deformation and dynamic properties. To this end, deformed configurations of soft pneumatic actuators are firstly discretized into ANCF-based beam elements. Based on this parameterization method, the dynamic model is derived by the principle of virtual work. After identifying model parameters, Newmark algorithm is utilized to solve the dynamic model in real-time, averagely consuming 6.76 s of a 10 s simulation. The derived dynamic model is experimental verified using a soft pneumatic actuator. The experimental results demonstrate that the maximum simulation errors of the tip remain below 2.5% of the actuator's length when the actuator is subjected to various pressure and tip loads. In addition, the overshoot behavior and period of vibration in the oscillations are also predicted by the dynamic model. Moreover, the dynamic model exhibits an average 46.53% reduction in simulation error compared with the static ANCF-based model. Overall, this work paves the way to a deeper insight to dynamic motion analysis of soft pneumatic actuators.

Keywords: soft pneumatic actuator, dynamic modeling, real-time simulation, absolute nodal coordinate formulation

## 1. Introduction

Soft actuators made from elastic materials exhibit superior flexibility and compliance compared to traditional rigid robots [1–3]. These inherent characteristics endow soft actuators with substantial potential across diverse domains [4–7]. Dynamic models are essential for widening soft actuators' applications because of their usage in dynamic simulation, design validation, and controller designs [1, 8]. Due to their continuous deformation without discrete joints, the efficient and accurate dynamic simulation of soft actuators is still challenging.

For soft actuators with infinite degree of freedom, the most-adopted dynamic modeling method is finite element method (FEM). In FEM, the dynamic model is calculated by numerically integrating forces through all elements and is expressed by a set of ordinary differential equations (ODEs). Commercial FEM software (such as Abaqus and ANSYS [9–11]) and open-source FEM packages (such as SOFA [12]

* Author to whom any correspondence should be addressed.

and Sorotoki [13]) are wildly employed to investigate the dynamic response of soft actuators. However, accurately simulating large deformation necessitates massive elements and small step sizes, leading to a heavy computation burden of FEM [14].

To enhance the computational efficiency, some analytical modeling techniques simplify soft actuators' shapes into slender rods with constant cross sections. Generally, these models can be roughly classified into two categories, i.e. piecewise constant curvature (PCC) models and variable curvature models. The well-known PCC models describe actuators' shapes by a series of circular arcs, and each arc is defined by three coordinates (i.e. curvature, curve length, and bending angle) [15]. By incorporating the PCC theory with the pseudo-rigid-body model or the lump section model [16, 17], dynamic models of soft actuators are derived in the form of second order ODEs. This method significantly reduces the number of configuration parameters, thus effectively decreasing calculation time. Despite these advantages, the PCC assumption is frequently violated in practical scenarios, especially when external forces (such as gravity and tip loads) are non-negligible.

To overcome the limitation of the PCC assumption, variable curvature models are proposed. These models are generally based on classic beam theories (such as Euler–Bernoulli beam theory [18] and Kirchhoff beam theory [19]) or continuum mechanics (such as Cosserat Rod theory [20]). By establishing mechanical equilibrium equations for an infinitesimal section, the dynamic models are expressed by high order PDEs in terms of time and reference arc length [21]. Extensive calculation algorithms are proposed to solve these dynamic models. For example, integration along the length and the time are calculated by fourth-order Runge Kutta and BDF-$\alpha$ algorithm, respectively [20]. Moreover, through the geometric variable-strain or piecewise constant-strain approach [22, 23], the Cosserat rod-based model is reduced to a set of ODEs and further calculated by Runge Kutta algorithms. In summary, most existing dynamic models focus on improving prediction accuracy by discretizing soft actuators into small elements [24, 25]. Notably, these menthods usually increase computation burden and lead to low computation efficiency. Althought some models also try to reduce the computation time, they generally rely on some impractical simplifying assumptions such as neglecting external forces [26] or actuation forces [27]. Therefore, it is still elusive to achieve computationally efficient simulation without the cost of model complexity and calculation inaccuracy.

Besides the mentioned variable curvature models, another continuum-based modeling approach, absolute nodal coordinate formulation (ANCF), has recently emerged for soft actuator modeling [28–30]. This model demonstrates both prediction accuracy and computational efficiency for various kinds of soft actuators (such as soft continuum actuators [28], soft parallel actuators [29], and soft bellow actuators [30]). The state-of-the-art ANCF models of soft actuators mainly focus on static analysis [28–30] or the theoretical presentation of dynamic cases [31]. Inspired by these achievements, we aim to take a further step by deriving an ANCF-based dynamic model for soft actuators and then verify it experimentally.

In this paper, we extend our previously proposed static model [28] into a dynamic model which further takes the inertia forces and the damping forces into consideration. To this end, variable curvature configurations of soft actuators are firstly parameterized by ANCF method. Then, an ordinary differential dynamic model is derived, which incorporates static forces, inertial forces, damping forces, and boundary constraints (BCs). To identifying model parameters, a series of experiments are designed and conducted. With determined parameters, the Newmark method is utilized to solve the developed dynamic model in real-time, consuming 6.76 s of a 10 s dynamic simulation. The simulation accuracy of the developed dynamic model is experimentally verified using a soft actuator. The experimental results demonstrate that, when actuated by sinusoidal control pressure, the dynamic model can achieve an average 46.53% reduction in average simulation error compared with the ANCF-based static model. Under the sweep frequency control pressure, the simulation error of the tip is less than 2.5% of the soft actuator's length. When subjected to complex actuation pressure and varying tip loads, the maximum simulation error is approximately 2% of the soft actuator's length. In addition, the dynamic model is capable of simulating the transition stage after releasing a tip load.

The main contributions of this work are summarized as follows.

(1) We present a ANCF-based dynamic model for a variable curvature soft pneumatic actuator. The derived model incorporates inertia dynamics and damping forces which quasi-static models typically neglect. Further, we employ an implicit integration algorithm to enable real-time dynamic simulation.
(2) We design parameter identification experiments for the bending stiffness, the damping coefficient, and dynamic simulation parameters. Based on the identified parameters, the developed dynamic model is experimentally verified using soft pneumatic actuators.

The reminder of this article is organized as follows. Section 2 presents the applied soft actuators and derives the dynamic model based on ANCF. Section 3 introduces the numerical calculation algorithm. In section 4, parameter identification experiments and model validation experiments are presented. Section 5 concludes this article.

## 2. Dynamic modeling of soft pneumatic actuators

In this section, we firstly introduce the structure and cross-sectional parameters of the applied soft pneumatic actuators. Then, we explicitly explain the ANCF-based parameterization of the variable curvature configurations and then derive the dynamic model. Finally, the calculation algorithm of the derived dynamic model is presented.

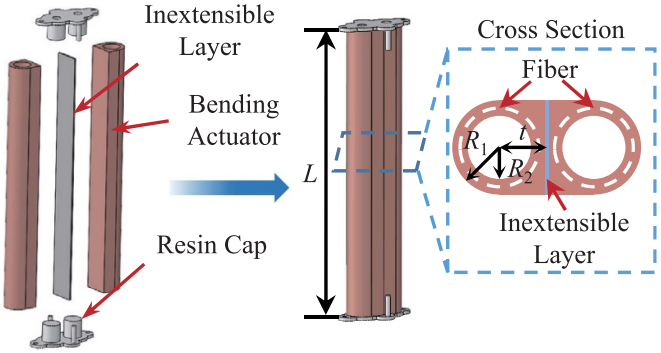


**Figure 1.** (left) Schematic illustration of the applied soft pneumatic actuator. (right) The cross section and geometric parameters presented.

### 2.1. Structure of soft pneumatic actuators

The applied soft actuator (shown in figure 1) is composed of two soft fiber-reinforced bending actuators. By inflating one chamber, the soft actuator can present bidirectional bending. Each fiber-reinforced bending actuator is fabricated through molding the inner rubber tube (Elastosil M4601, Wacker Chemie AG, Germany), fiber winging, and molding the outer rubber tube [28]. Then, two soft fiber-reinforced actuators, an inextensible layer between them, and two resin caps are assembled using silicon adhesive (Sil-Poxy, Smooth-on, USA). The length $L$ of the soft actuator is 175 mm. The geometrical parameters of the cross-section (shown in figure 1) are $R_1 = 9$ mm, $R_2 = 6$ mm, and $t = 9$ mm. Bending is the main deformation for this soft actuator, and torsion and shearing can be neglected [28].

### 2.2. Kinematics

To parameterize the configuration of the deformed soft actuator, we employ the ANCF method. In principle, a soft actuator is discretized into $n$ elements by $(n+1)$ nodes which are set along the centerline of the soft actuator (as illustrated in figure 2). The $i$-th element starts from the $i$-th node and terminates at the $(i+1)$-th node. In the $i$-th element with an undeformed length $L$, the global position of an arbitrary point $\mathbf{r}(x) \in \mathbb{R}^2$ is a function of the arc length $x \in [0, L]$ which is defined in the underformed configuration. In the ANCF method, the generalized coordinates of the $i$-th node $\mathbf{q}_i \in \mathbb{R}^4$and $(i+1)$-th node $\mathbf{q}_{i+1} \in \mathbb{R}^4$ are

$$\begin{cases} \mathbf{q}_i = \left[\mathbf{r}^T(0) \quad \mathbf{r}_x^T(0)\right]^T \\ \mathbf{q}_{i+1} = \left[\mathbf{r}^T(L) \quad \mathbf{r}_x^T(L)\right]^T \end{cases}, \tag{1}$$

where $()_x$ denotes a derivative with respect to $x$ [32]. The generalized coordinate of the $i$-th element $\mathbf{q}^i \in \mathbb{R}^8$ can be written as

$$\mathbf{q}^i = \left[\mathbf{q}_i^T \quad \mathbf{q}_{i+1}^T\right]^T = \left[q_1^i \quad \cdots \quad q_8^i\right]^T. \tag{2}$$

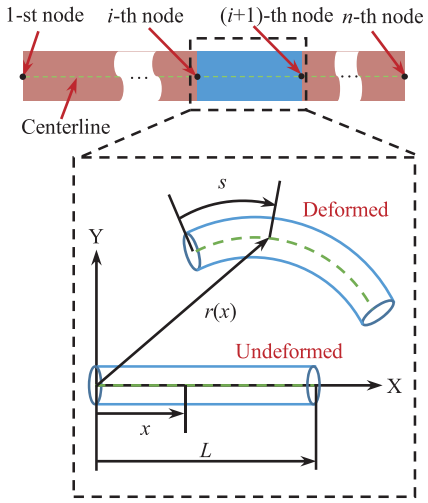


**Figure 2.** Schematic illustration of the configuration description of the soft actuator based on ANCF. The soft actuator can be discretized into $n$ elements. Each point is parameterized by the arc length $x$, defined in the undeformed configuration.

The global position $\mathbf{r}(x)$ can then be expressed by $\mathbf{q}^i$ as

$$\mathbf{r}(x) = \mathbf{S}(x)\,\mathbf{q}^i, \tag{3}$$

where $\mathbf{S}(x) \in \mathbb{R}^{2\times 8}$is the shape function. The explicit expression of $\mathbf{S}(x)$ is expressed as

$$\begin{aligned} &\mathbf{S}(x) = \begin{bmatrix} s_1\mathbf{I}_2 & s_2\mathbf{I}_2 & s_3\mathbf{I}_2 & s_4\mathbf{I}_2 \end{bmatrix} \\ &\begin{cases} s_1 = 1 - 3\xi^2 + 2\xi^3 \\ s_2 = L\left(\xi - 2\xi^2 + \xi^3\right) \\ s_3 = 3\xi^2 - 2\xi^3 \\ s_4 = L\left(-\xi^2 + \xi^3\right) \end{cases}, \end{aligned} \tag{4}$$

where $\xi = x/L$ and $\mathbf{I}_2$ is a $2\times 2$ identity matrix. By combining generalized coordinates of all nodes, the configuration coordinate of the soft actuator $\mathbf{q} \in \mathbb{R}^{4(n+1)}$is given as

$$\mathbf{q} = \begin{bmatrix} \mathbf{q}_1^T & \cdots & \mathbf{q}_{n+1}^T \end{bmatrix}^T = \begin{bmatrix} q_1 & q_2 & \cdots & q_{4n+3} & q_{4n+4} \end{bmatrix}^T. \tag{5}$$

### 2.3. Dynamics

Based on the principle of virtual work, the dynamic equation without the dissipate term of the $i$-th element is as follows

$$\mathbf{M}^i\ddot{\mathbf{q}}^i + \mathbf{Q}_e^i = \mathbf{Q}_f^i, \tag{6}$$

where the dot symbol denotes a derivative with respect to time [33]. $\mathbf{M}^i$, $\mathbf{Q}_e^i$, and $\mathbf{Q}_f^i$ represents the mass matrix, the generalized elastic forces, and the generalized external forces, respectively.

The mass matrix $\mathbf{M}^i$ is firstly derived by the kinetic energy. We assume that the material is uniformly distributed along the

centerline and that the cross section is rigid. The kinetic energy of the $i$th element $T^i$ takes the form

$$T^i = \frac{1}{2}\int_0^L \rho A \dot{\mathbf{r}}^T \dot{\mathbf{r}} \mathrm{d}x = \frac{1}{2}\left(\dot{\mathbf{q}}^i\right)^T \left(\rho A \int_0^L \mathbf{S}(x)^T \mathbf{S}(x)\,\mathrm{d}x\right) \dot{\mathbf{q}}^i = \frac{1}{2}\left(\dot{\mathbf{q}}^i\right)^T \mathbf{M}^i \dot{\mathbf{q}}^i, \tag{7}$$

where $\rho$ and $A$ are the density and the area of the cross section, respectively. Therefore, the constant mass matrix $\mathbf{M}^i$ can be written as

$$\mathbf{M}^i = \rho A \int_0^L \mathbf{S}(x)^T \mathbf{S}(x)\,\mathrm{d}x. \tag{8}$$

The generalized elastic forces $\mathbf{Q}_e^i$ can be calculated from the elastic potential energy. As shown in figure 1, the applied soft pneumatic actuator is composed of silicone rubber, fiber, and an inextensible layer. If the soft pneumatic actuator is treated as a multi-material structure, the elastic potential energies of each material should be calculated separately and then summed up to obtain the total elastic potential energy [34]. This method can largely increase the computation burden. To simplify the model and increase computation efficiency, the soft pneumatic actuator is modeled as a homogeneous incompressible material. For this homogeneous material, the equivalent mechanical parameters (i.e. bending stiffness and the damping coefficient) are used to ensure the model accuracy. These equivalent mechanical parameters are typically calibrated by experiments, which will be introduced in the next section. The elastic potential energy is solely attributed to the bending deformation. Under the assumption of constant bending stiffness $EI$, the elastic potential energy can be expressed as

$$U_b = \frac{1}{2}\int_0^L EI\kappa(x)^2 \mathrm{d}x, \tag{9}$$

where $\kappa(x)$ is the curvature. The length of the applied soft actuator is considered constant because of the presence of the inextensible layer. Consequently, the curvature $\kappa(x)$ can be approximated by

$$\kappa(x) = \|\mathbf{r}_{xx}\|, \tag{10}$$

where $()_{xx}$ denotes the second-order derivative with respect to $x$ [35]. To satisfy the inextensible condition during calculation, we use the penalty function donated as

$$U_p = \frac{1}{2}\int_0^L k\varepsilon(x)^2 \mathrm{d}x, \tag{11}$$

where $k$ is the penalty constant, and $\varepsilon$ defined in (12) is the Green strain tensor

$$\varepsilon(x) = \frac{1}{2}\left(\mathbf{r}_x^T \mathbf{r}_x - 1\right). \tag{12}$$

By adding (9) and (11) together, the total elastic energy $U$ is calculated by

$$U = U_b + U_p = \frac{1}{2}\int_0^L EI\kappa(x)^2 \mathrm{d}x + \frac{1}{2}\int_0^L k\varepsilon(x)^2 \mathrm{d}x. \tag{13}$$

Utilizing the principle of virtual work, generalized elastic forces $\mathbf{Q}_e^i$ are determined as

$$\mathbf{Q}_e^i = \left(\frac{\partial U}{\partial \mathbf{q}^i}\right)^T = \int_0^L \left(EI\mathbf{S}_{xx}(x)^T \mathbf{S}_{xx}(x) + k\varepsilon \mathbf{S}_x(x)^T \mathbf{S}_x(x)\right) \mathrm{d}x \mathbf{q}^i. \tag{14}$$

Generalized external forces $\mathbf{Q}_f^i$ are caused by the payload, gravity, and the actuation force. For the payload $m$ applied at $x_p$, the generalized payload forces $\mathbf{Q}_m^i$ are given by

$$\mathbf{Q}_m^i = \left(\frac{\partial \mathbf{r}(x_p)}{\partial \mathbf{q}^i}\right)^T m\mathbf{g} = \mathbf{S}(x_p)^T m\mathbf{g}, \tag{15}$$

where $\mathbf{g}$ is the gravitational acceleration. Similarly, the generalized gravity forces $\mathbf{Q}_g^i$ are given by

$$\mathbf{Q}_g^i = \rho A \int_0^L \left(\frac{\partial \mathbf{r}(x)}{\partial \mathbf{q}^i}\right)^T \mathbf{g}\mathrm{d}x = \rho A \int_0^L \mathbf{S}(x)^T \mathbf{g}\mathrm{d}x. \tag{16}$$

When the cross section is assumed to be rigid, the deformation effect of actuated pressure P can be simplified as a pair of torque ($-M = -\pi R_2^2 Pt$ at $x = 0$ and $M = \pi R_2^2 Pt$ at $x = l$) acting at the two nodes [28, 36]. The generalized actuation forces $\mathbf{Q}_a^i$ is given by

$$\mathbf{Q}_a^i = -M\left(\mathbf{n}_1 \times \frac{\partial \mathbf{n}_1}{\partial \mathbf{q}^i}\right)^T + M\left(\mathbf{n}_2 \times \frac{\partial \mathbf{n}_2}{\partial \mathbf{q}^i}\right)^T \quad \begin{cases} \mathbf{n}_1 = \frac{1}{\sqrt{\left(q_3^i\right)^2 + \left(q_4^i\right)^2}} \begin{bmatrix} q_3^i & q_4^i \end{bmatrix}^T \\ \mathbf{n}_2 = \frac{1}{\sqrt{\left(q_7^i\right)^2 + \left(q_7^i\right)^2}} \begin{bmatrix} q_7^i & q_8^i \end{bmatrix}^T \end{cases}, \tag{17}$$

where $\mathbf{n}_1$ and $\mathbf{n}_2$ are the unit axial vectors at two nodes. Considering the inextensible condition ($\|\mathbf{r}_x(x)\| = 1$), the equation (17) is simplified as

$$\mathbf{Q}_a^i = \begin{bmatrix} \mathbf{0}_2 & Mq_4^i & -Mq_3^i & \mathbf{0}_2 & -Mq_8^i & Mq_7^i \end{bmatrix}^T, \tag{18}$$

where $\mathbf{0}_2$ denotes a two-dimensional row vector. By adding (15), (16), and (18) together, the generalized external forces $\mathbf{Q}_f^i$ are given by

$$\mathbf{Q}_f^i = \mathbf{Q}_m^i + \mathbf{Q}_g^i + \mathbf{Q}_a^i. \tag{19}$$

The generalized coordinate of the $i$-th element $\mathbf{q}^i$ and the configuration coordinate of the soft actuator $\mathbf{q}$ satisfy

$$\mathbf{q}^i = \mathbf{B}^i \mathbf{q}, \tag{20}$$

where $\mathbf{B}^i \in \mathbb{R}^{8\times 4(n+1)}$ is the Boolean matrix [37]. Using the Boolean matrix, the dynamic model of the soft actuator can be derived as

$$\mathbf{M}\ddot{\mathbf{q}} + \mathbf{Q}_e = \mathbf{Q}_f, \tag{21}$$

where

$$\begin{aligned}\mathbf{M} &= \sum_{i=1}^{n} \mathbf{B}^{iT}\mathbf{M}^i\mathbf{B}^i \\ \mathbf{Q}_e &= \sum_{i=1}^{n} \mathbf{B}^{iT}\mathbf{Q}_e^i \\ \mathbf{Q}_f &= \sum_{i=1}^{n} \mathbf{B}^{iT}\mathbf{Q}_f^i\end{aligned}. \tag{22}$$

Moreover, we further complete (21) by introducing the Rayleigh damping term $c\mathbf{M}\dot{\mathbf{q}}$ [38] and constrain equations $\mathbf{C}(\mathbf{q}) = \mathbf{0}$:

$$\mathbf{f} = \begin{bmatrix}\mathbf{f}_1 \\ \mathbf{f}_2\end{bmatrix} = \begin{bmatrix}\mathbf{M}\ddot{\mathbf{q}} + c\mathbf{M}\dot{\mathbf{q}} + \mathbf{Q}_e - \mathbf{Q}_f + \mathbf{C}_\mathbf{q}^T\boldsymbol{\lambda} \\ \mathbf{C}\end{bmatrix} = \mathbf{0}, \tag{23}$$

where $c$ is the damping coefficient, $\mathbf{C}_\mathbf{q}$ is the Jacobian matrix of constrain equations with respect to the configutaion coordinate, and $\boldsymbol{\lambda}$ is the Lagrange multiplier. The derived dynamic model is in the Euler-Lagrangian form.

## 3. Numerical calculation

Since the derived dynamic model (23) is a highly stiff system, explicit integration schemes can lead to heavy computation burden due to the Courant–Friedrichs–Lewy condition [39]. Therefore, the Newmark method, one kind of implicit integration schemes, is applied to perform the dynamic simulation [40].

In the Newmark method, the time-integration schemes of the position vector $\mathbf{q}_{n+1}$ and the velocity vector $\dot{\mathbf{q}}_{n+1}$ at time $t_{n+1}$ are as follows

$$\begin{cases}\mathbf{q}_{n+1} = \mathbf{q}_n + \Delta h\dot{\mathbf{q}}_n + 0.5\Delta h^2\left[(1-2\beta)\ddot{\mathbf{q}}_n + 2\beta\ddot{\mathbf{q}}_{n+1}\right] \\ \dot{\mathbf{q}}_{n+1} = \dot{\mathbf{q}}_n + \Delta h\left[(1-\gamma)\ddot{\mathbf{q}}_n + \gamma\ddot{\mathbf{q}}_{n+1}\right]\end{cases}, \tag{24}$$

where $\Delta h = t_{n+1} - t_n$ is the integration time-step, and $\beta$ and $\gamma$ are defined parameters. To obtain the second order convergence property, $\beta$ and $\gamma$ in this work are set to 0.25 and 0.5, respectively [40].

In each integration step, the acceleration vector $\ddot{q}_{n+1}$ and the Lagrange multiplier $\boldsymbol{\lambda}_{n+1}$ in (23) are calculated by the Newton–Raphson algorithm [41] with the following iterations:

$$\begin{bmatrix}\Delta\ddot{\mathbf{q}}_{n+1} \\ \Delta\boldsymbol{\lambda}_{n+1}\end{bmatrix}^{(k+1)} = \begin{bmatrix}\Delta\ddot{\mathbf{q}}_{n+1} \\ \Delta\boldsymbol{\lambda}_{n+1}\end{bmatrix}^{(k)} - \begin{bmatrix}\frac{\partial\mathbf{f}_1}{\partial\ddot{\mathbf{q}}_{n+1}} & \frac{\partial\mathbf{f}_1}{\partial\boldsymbol{\lambda}_{n+1}} \\ \frac{\partial\mathbf{f}_2}{\partial\ddot{\mathbf{q}}_{n+1}} & \frac{\partial\mathbf{f}_2}{\partial\boldsymbol{\lambda}_{n+1}}\end{bmatrix}^{-1}\begin{bmatrix}\mathbf{f}_1 \\ \mathbf{f}_2\end{bmatrix}^{(k)}. \tag{25}$$

Each submatirx in the Jacobian matrix can be calculated as:

$$\begin{aligned}\frac{\partial\mathbf{f}_1}{\partial\ddot{\mathbf{q}}_{n+1}} &= \mathbf{M} + \gamma\Delta hc\mathbf{M} + \beta\Delta h^2\left(\frac{\partial\mathbf{Q}_e}{\partial\mathbf{q}_{n+1}} - \frac{\partial\mathbf{Q}_a}{\partial\mathbf{q}_{n+1}}\right), \\ \frac{\partial\mathbf{f}_1}{\partial\boldsymbol{\lambda}_{n+1}} &= \mathbf{C}_q^T, \frac{\partial\mathbf{f}_2}{\partial\ddot{\mathbf{q}}_{n+1}} = \beta\Delta h^2\mathbf{C}_q, \frac{\partial\mathbf{f}_2}{\partial\boldsymbol{\lambda}_{n+1}} = \mathbf{0}.\end{aligned} \tag{26}$$

Using equations (22), $\partial\mathbf{Q}_e/\partial\mathbf{q}$ and $\partial\mathbf{Q}_a/\partial\mathbf{q}$ are calculated as

$$\frac{\partial\mathbf{Q}_e}{\partial\mathbf{q}} = \sum_i \mathbf{B}^{iT}\frac{\partial\mathbf{Q}_e^i}{\partial\mathbf{q}^i}, \frac{\partial\mathbf{Q}_a}{\partial\mathbf{q}} = \sum_i \mathbf{B}^{iT}\frac{\partial\mathbf{Q}_a^i}{\partial\mathbf{q}^i}, \tag{27}$$

where

$$\frac{\partial\mathbf{Q}_e^i}{\partial\mathbf{q}^i} = \int_0^L \left(EI\mathbf{S}_{xx}^T\mathbf{S}_{xx} + k\varepsilon\mathbf{S}_x^T\mathbf{S}_x + k\mathbf{S}_x^T\mathbf{S}_x\mathbf{q}^i\mathbf{q}^{iT}\mathbf{S}_x^T\mathbf{S}_x\right)\mathrm{d}x, \tag{28}$$

$$\frac{\partial\mathbf{Q}_a^i}{\partial\mathbf{q}_{n+1}^i} = \begin{bmatrix}0&0&0&0&0&0&0&0\\0&0&0&0&0&0&0&0\\0&0&0&M&0&0&0&0\\0&0&-M&0&0&0&0&0\\0&0&0&0&0&0&0&0\\0&0&0&0&0&0&0&0\\0&0&0&0&0&0&0&-M\\0&0&0&0&0&0&M&0\end{bmatrix}. \tag{29}$$

Since the Jacobian matrix is time-consuming to calculate, it is only updated in the beginning of each Newton iteration. In addition, integrals are numerically calculated by Gauss-Legendre quadrature to improve the computational efficiency.

## 4. Experiments

In this section, the experimental platform is firstly described. Then, parameter identification experiments are introduced. Finally, validation experiments and corresponding results are presented and analyzed. It should be noted that the actuation frequencies of all experiments are restricted within 1.6 Hz to avoid exciting the vibration. The threshold frequency (i.e. 1.6 Hz) is determined by the frequency sweep test.

### 4.1. Experimental platform

The experimental platform is demonstrated in figure 3. Specifically, the control signal is sent from a control module (dSPACEDS1103 board, dSPACE, Paderborn, Germany) to the pneumatic system. After receiving the control signal, the pneumatic system outputs compressed gas, and the pressure is measured by the embedded pressure sensor (Type511, HUBA, Switzerland). The tip displacements of the soft actuator are simultaneously measured by a motion capture system (Prime 13, OptiTrack, USA) and saved by the computer in real-time.

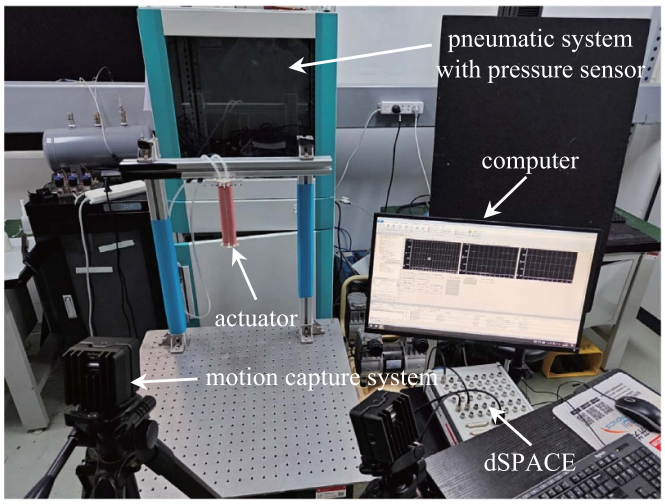


**Figure 3.** The experimental platform.

### 4.2. Parameter identification experiments

In the developed dynamic model, the bending stiffness $EI$ and the damping coefficient $c$ need to be identified. Besides, to achieve accurate and efficient dynamic simulation, numerical calculation parameters (i.e. the number of elements $n$ and the integration time-step $\Delta h$) also need to be determined. Therefore, we conduct the parameter identification experiments for these parameters.

To identify the bending stiffness $EI$, the soft actuator is horizontally clamped without actuation (shown figure 4(a)). A 30 g weight is attached to the tip of the soft actuator. In this circumstance, the bending deformation of the soft actuator is only caused by gravity and the attached weight. The vertical displacement of the tip $\Delta y = 34.37$ mm is measured by the OptiTrack system. Given a specific $EI$, the vertical displacement of the tip, denoted by $|q_{4n+2}|$, can also calculated by solving (23) when neglecting the generalized inertial forces, the generalized damping forces, and the generalized actuation forces. Consequently, the bending stiffness $EI$ can be identified by solving the following constrained optimization problem:

$$\begin{aligned} &\min_{EI} \left(\Delta y - |q_{4n+2}|\right)^2 \\ &\text{subject to } \begin{bmatrix} \mathbf{Q}_e - \mathbf{Q}_f + \mathbf{C}_\mathbf{q}^T \boldsymbol{\lambda} \\ \mathbf{C} \end{bmatrix} = \mathbf{0}. \end{aligned} \tag{30}$$

To ensure the accuracy of the calculation, the number of the elements $n$ is set to 15, and MATLAB implements the calculation. Figure 4(b) illustrates the relation between the bending stiffness and the simulated vertical displacement. Through this analysis, the bending stiffness $EI$ is identified as $0.0186\ \mathrm{N \cdot m^2}$.

To identify the damping coefficient $c$, the soft actuator is vertically clamped without tip weight. A 10 s sinusoidal pressure with the frequency of 1.6 Hz is applied to actuate the soft actuator. The tip positions of the soft actuator are recorded by the OptiTrack system. The control frequency of the dSPACE board is 50 Hz, and the sampling frequency of the OptiTrack system is 100 Hz. Given a specific actuated pressure, the tip

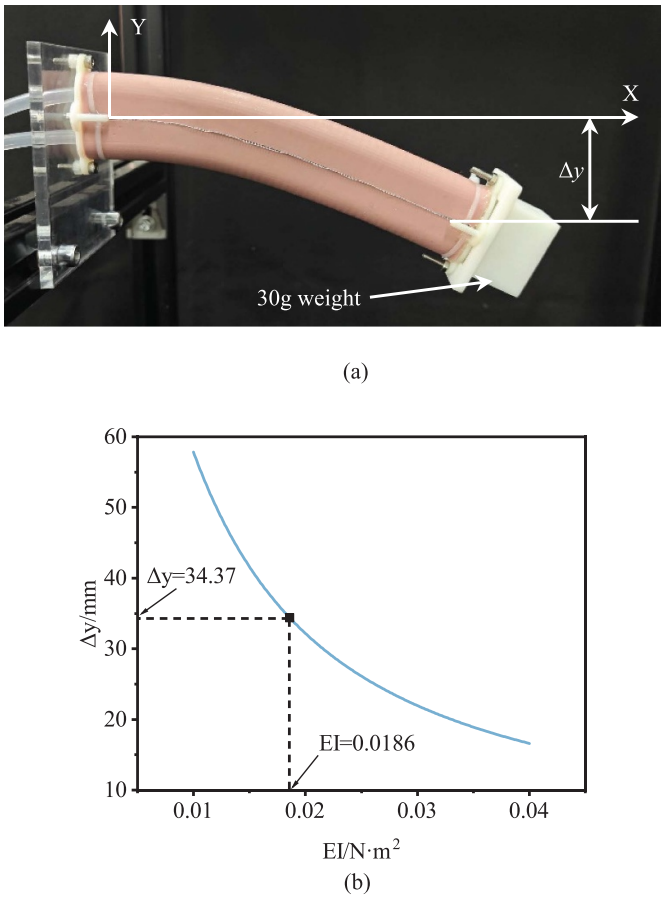


**Figure 4.** Experimental setup and results of the bending stiffness identification. (a) Experimental setup. A 30 g weight is attached to the tip of the soft actuator, and the vertical displacement of the tip $\Delta y$ is measured. (b) The relation between the bending stiffness and the simulated vertical displacement with a 30 g tip load.

response can be calculated by the presented dynamic simulation. Therefore, the damping coefficient can be identified by minimizing the root mean square error (RMSE) between recorded tip positions and simulated tip positions, which is defined as

$$e = \sqrt{\frac{1}{N}\sum_{i=1}^{N} \left(\mathbf{p}_r^i - \mathbf{p}_s^i\right)^2}, \tag{31}$$

where $N$ is the total number of recorded data, and $\mathbf{p}_r^i$ and $\mathbf{p}_s^i$ are $i$-th recorded and $i$-th simulated positions, respectively. To ensure the accurate calculation, the number of the elements $n$ and the integration time-step $\Delta h$ are set to 15 and 0.1 ms, respectively. Figure 5 illustrates the relation between the damping coefficient and the RMSE. It is clear that the damping coefficient c is identified as $2.4\ \mathrm{N\,s\,m^{-1}}$.

The recorded dynamic response under actuation frequency of 1.6 Hz is also used to determine the simulation parameters. Different numbers of elements (ranging from 1 to 7) and different integration time steps ($\Delta h_1 = 0.1$ ms, $\Delta h_2 = 0.5$ ms, $\Delta h_3 = 1$ ms) are systematically tested. Figure 6 presents the

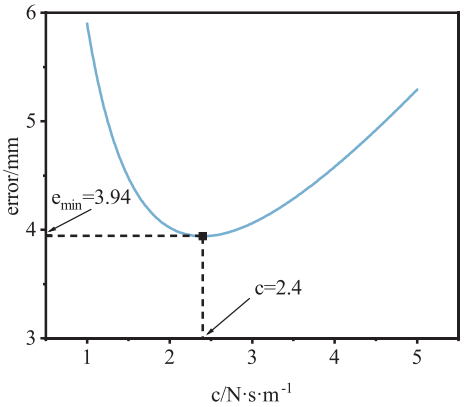


**Figure 5.** The relation between the damping ratio and the average simulation error when the 1.6 Hz input pressure is applied.

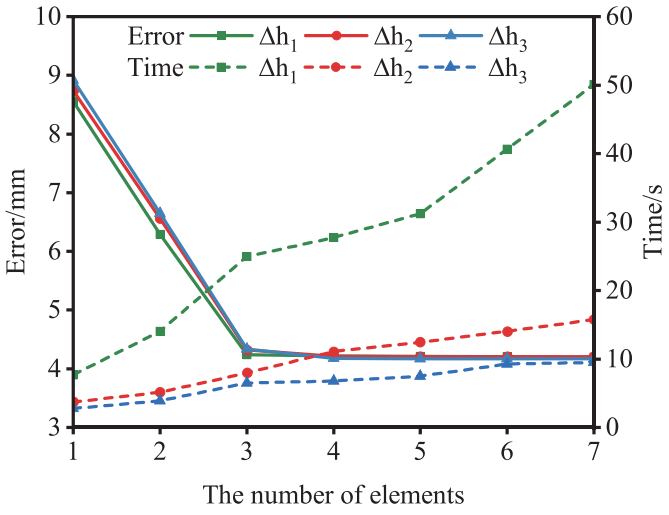


**Figure 6.** Average simulation error (solid line) and computation time (dashed line) against the number of the discrete elements and the integration time-step.

experimental results, comparing simulated RMSEs and computation time. The simulated RMSE demonstrates a decreasing trend as the number of elements $n$ increases. However, this improvement tends to plateau when the number of elements exceeds 4. Conversely, the computation time exhibits a steady increase with an increasing number of elements. Notably, different integration time steps show few influence on the simulated RMSEs. Therefore, to guarantee accurate and efficient dynamic simulation, the number of elements $n$ and the integration time-step $\Delta h$ are identified as 4 and 1 ms, respectively. With this set of parameters, the calculation required 6.76 s for a 10 s simulation, which is already real-time.

### 4.3. Validation experiments

*4.3.1. Simulation under sinusoidal pressure.* The developed dynamic model is firstly validated using sinusoidal pressure. To demonstrate its ability in dynamic simulation, the ANCF-based static model [28] is utilized as a benchmark. The soft actuator is vertically clamped without tip weight. One chamber is actuated by sinusoidal pressure with frequencies of 0.4 Hz, 0.7 Hz, and 1.0 Hz, while the actuation pressure of the other chamber maintains 0 kPa. Displacements of the actuator tip are recorded by the OptiTrack system during actuation. Using the dynamic simulation RMSE $e_d$ and the static simulation RMSE $e_s$, the error reduction rate $r_e$ is defined as

$$r_e = \left(1 - \frac{e_d}{e_s}\right) \times 100\%. \tag{32}$$

The simulation performance of both the dynamic model and the quasi-static model is presented in figure 7. The simulation errors of the static model are 4.4633 mm (0.4 Hz), 5.0139 mm (0.7 Hz), and 7.2328 mm (1.0 Hz), respectively. In contrast, the simulation errors of the dynamic model are 2.7712 mm (0.4 Hz), 2.6919 mm (0.7 Hz), and 3.2290 mm (1.0 Hz), indicating error reductions of 37.91%, 46.31%, and 55.36%, respectively. The experimental results emphasize the limitation of the static model in predicting output phase lag, which is induced by the dynamic property of the soft actuator. Therefore, the simulation performance of the static model dramatically degrades as the frequency increases. On the contrary, the dynamic model predicts the output phase lag as illustrated in figure 7, thereby achieving more accurate simulation results.

*4.3.2. Simulation under complex pressure and tip loads.* The dynamic model is further validated under the condition that the soft actuator is subject to complex pressure and varying tip loads. Firstly, the soft actuator is vertically clamped without tip weight. Five reflective makers are uniformly placed along the centerline of the soft actuator to capture whole configurations. One chamber is actuated by a sweep frequency pressure (ranging from 0.01 Hz to 1.6 Hz in 8 seconds), while the other remains uninflated. Figure 8(a) illustrates the real tip response and the simulated one. The RMSE of the dynamic simulation is 3.84 mm, less than 2.5% of the soft actuator's length. Moreover, the presented dynamic model effectively captures the output phase lag within the applied frequency range. The recorded and simulated configurations at different times are showcased in figure 8(b). The simulated configurations closely align with the recorded ones, verifying the presented dynamic model.

After the sweep frequency pressure experiment, various known weights, ranging from 0 g to 50 g, are applied to the tip. Both chambers of the soft actuator are actuated by complex control pressure (shown in figure 8(c)). Each control pressure is the superposition of sinusoidal pressures with different frequencies (below 1.6 Hz) and phases. As presented by table 1, the average simulation RMSE of the dynamic model is 2.69 mm, equivalent to 1.54% of the soft actuator's length. Notably, there is no significant error increase when different tip loads are applied. The simulated tip response and experimental results with a 20 g applied tip load are exemplified in figure 8(d). The simulated data are roughly consistent with the experimental results, validating the accuracy of the dynamic model.

Finally, the soft actuator is horizontally fixed, and the same actuation pressure and tip loads (from 0 g to 50 g) are imposed.

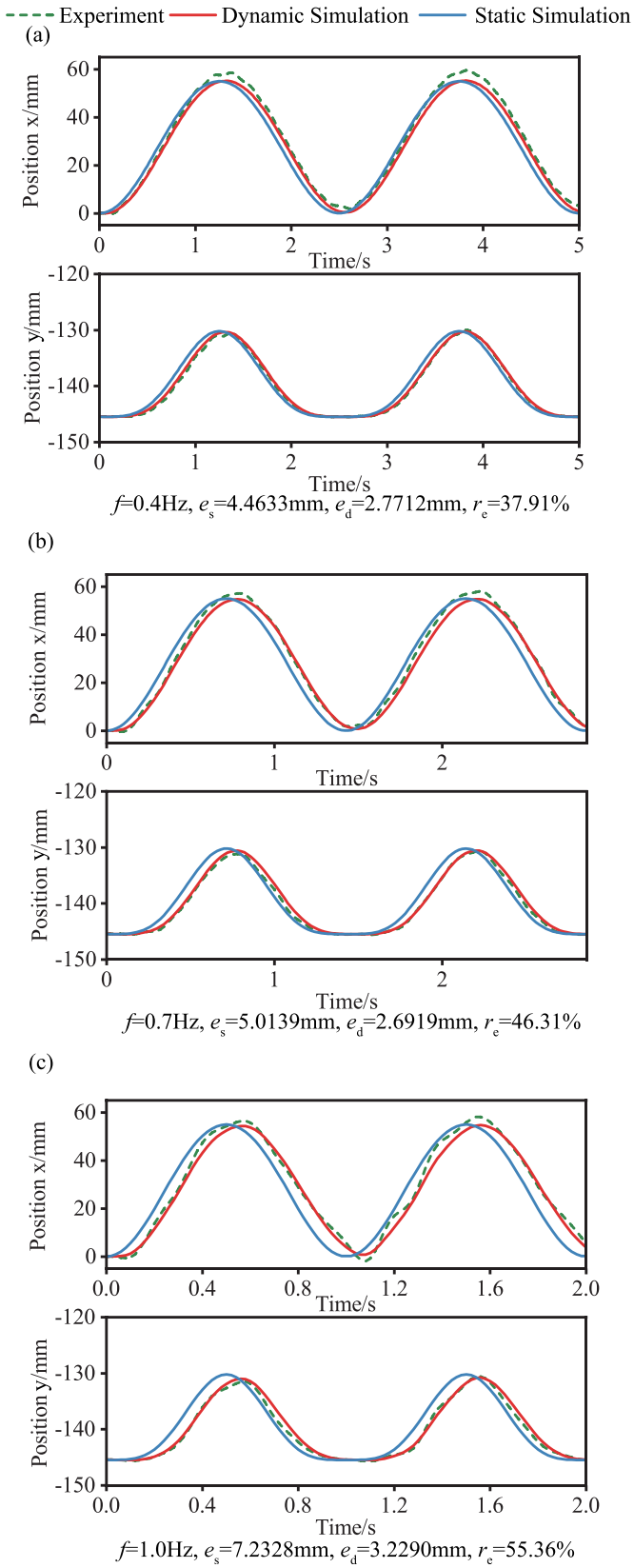


**Figure 7.** Comparison of the tip response between the dynamic simulation (red line) and the static simulation (blue line) under the input pressure frequency of (a) 0.4 Hz, (b) 0.7 Hz, and (c) 1.0 Hz.

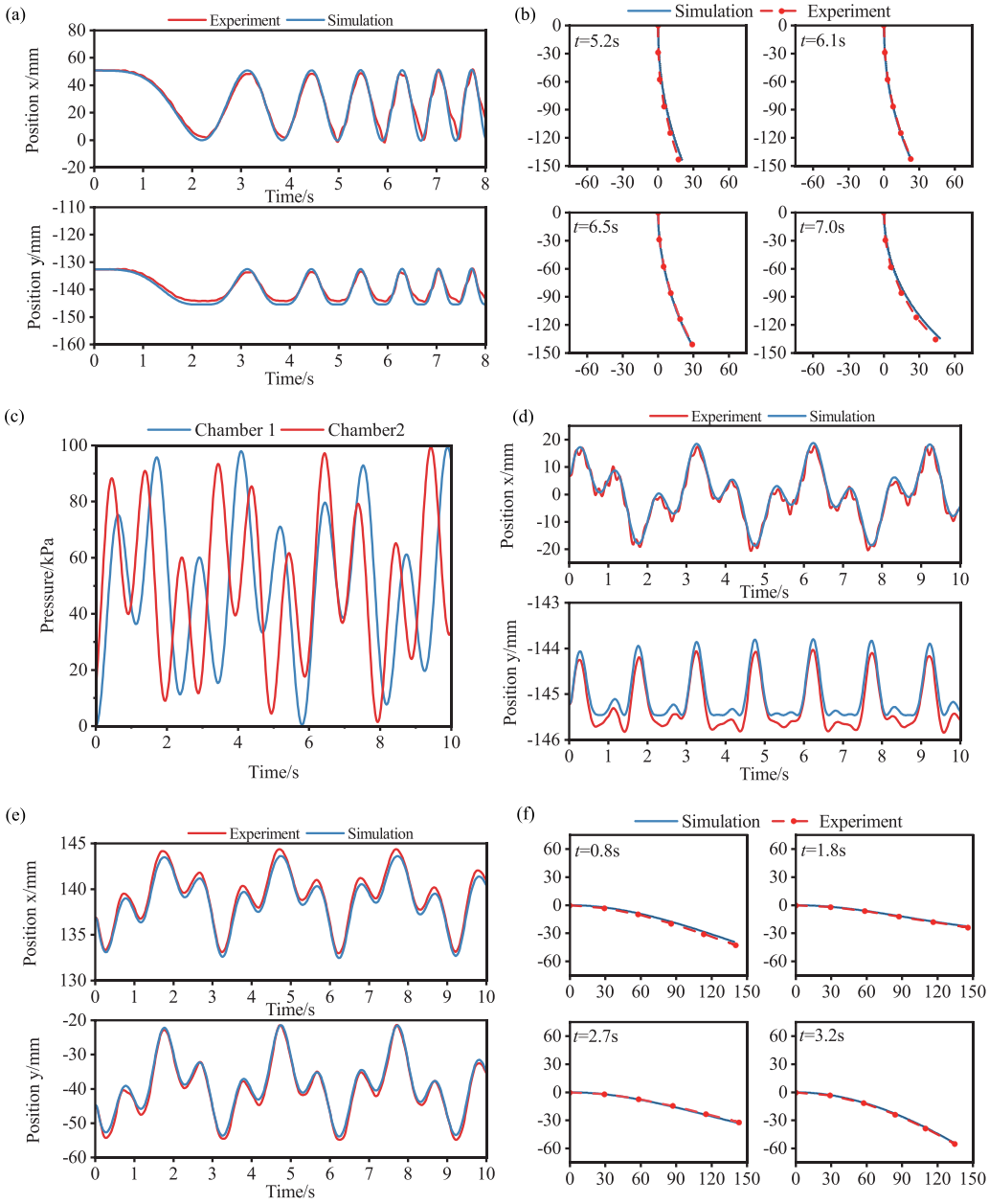


**Figure 8.** Experimental results of the model validation under complex actuation pressure. Experimental results of vertically fixed actuator under the sweep frequency pressure: (a) The predicted tip response and the collected displacement; (b) Predicted soft actuator shapes and the recorded results at different times (coordinate units: mm). (c) The complex pressure signal applied to chamber 1 and chamber 2. (d) The predicted tip response and the collected displacement when the soft actuator is vertically fixed with a 20 g tip load. Experimental results of horizontally fixed actuator under the complex actuation pressure and a 50 g tip load: (e) The predicted tip response and the collected displacement; (f) Predicted soft actuator shapes and the recorded results at different times (coordinate units: mm).

**Table 1.** Simulation RMSEs of the vertically clamped soft actuator.

| Tip Load(g) | RMSE(mm) |
|---|---|
| 0 | 2.9563 |
| 10 | 2.7775 |
| 20 | 2.7462 |
| 30 | 2.5361 |
| 40 | 2.4540 |
| 50 | 2.6545 |

**Table 2.** Simulation RMSEs of the horizontally clamped soft actuator.

| Tip Load(g) | RMSE(mm) |
|---|---|
| 0 | 3.1998 |
| 10 | 3.2572 |
| 20 | 3.3420 |
| 30 | 3.3407 |
| 40 | 3.4520 |
| 50 | 3.1897 |

As illustrated in table 2, the simulation RMSEs exhibit consistency across various tip loads, with a minimal error of 3.1897 mm and a maximal error of 3.4520 mm. Figure 8(e) showcases the simulated tip response and the experimental data when a 50 g tip load is applied to the horizontally fixed soft actuator. The simulation results are in good accordance with the experimental data. Additionally, figure 8(f) presents simulated and recorded configurations at different times. Even when the soft actuator undergoes large deformation (t = 3.2 s), the configuration can still be accurately predicted. In summary, the diverse results collectively validate the presented dynamic model.

*4.3.3. Simulation of oscillation.* In the experiment, the soft actuator is horizontally fixed, and a 100 g load is applied to the tip by a string. After the soft actuator reaches the equilibrium state, the string is cut suddenly (as shown in figure 9(a). Configurations of the soft actuator during the oscillation process are recorded using the OptiTrack system. Figure 9(b) illustrates the simulated transition stage of the tip after the 100 g load is suddenly released. The simulation result coincides approximately with the experimental result at the initial stage, in terms of the period of vibration and the overshoot behavior. The main manifestations of simulation error are slight differences in peak values and vibration frequencies that causes the phase shift. Possible reasons are nonlinear elastic forces, unmodeled dissipative forces, and neglected material viscosity. In summary, this experimental results show that the dynamic model can capture the dominant dynamic property of the soft actuator.

### 4.4. Diuscussion

Experiments demonstrate that the proposed dynamic model can accurately predict the deformed configurations under different actuation pressures. Compared to existing research, the proposed dynamic model incorporates both external forces and actuation forces. Meanwhile, real-time dynamic simulation is achieved by utilizing the Newmark algorithm and simplifying the model in two key ways. The first assumption is the simplified equation of the curvature due to the existence of the inextensible layer. The second assumption is to model the soft actuator as a homogeneous incompressible material with nominal material properties. Therefore, the proposed dynamic model is applicable to a wide range of soft

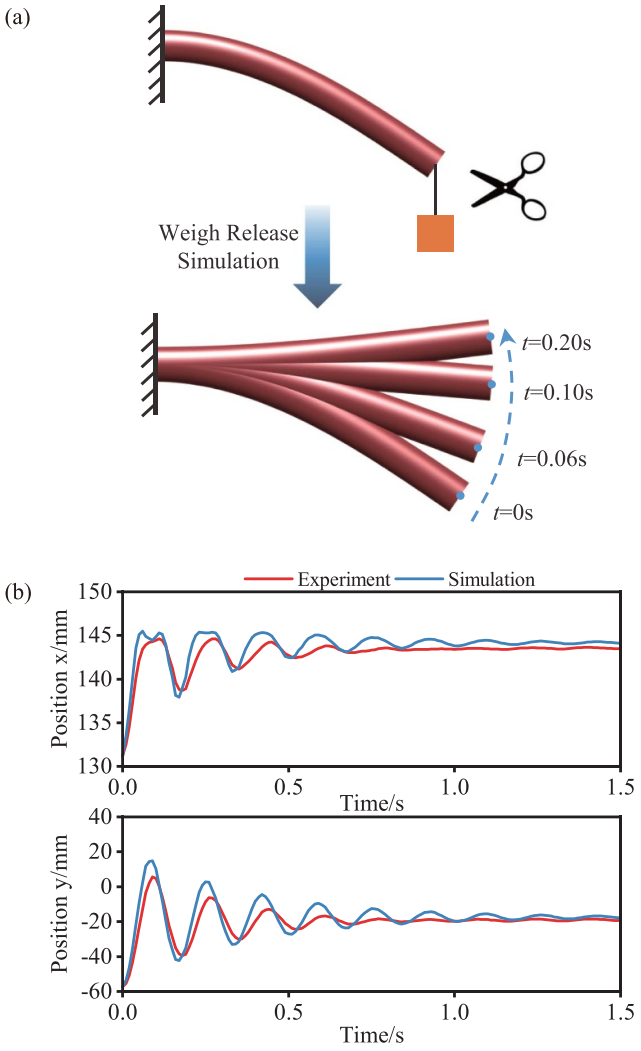


**Figure 9.** (a). Schematic illustration of the weight release scenario. (b). Tip response of the weight release scenario.

pneumatic actuators with limited length change, irrespective of their shapes, dimensions, and materials. Furthermore, the proposed dynamic model is verified under non-contact working scenarios. When operating in environments with obstacles and potential contact, contact constraints should be incorporated into the constraint equations $\mathbf{C}(\mathbf{q})$.

Additionally, the actuation frequencies of all validation experiments are within 1.6 Hz. For applications involving faster movements (such as locomotion and haptics) where soft actuators exhibit movements as rapid as 100 Hz, modifications to our dynamic model are necessary. Specifically, material viscosity (i.e. the tan delta of the elastomer) must be considered by changing the Rayleigh damping term into $(c_1\mathbf{M} + c_2\mathbf{K})\dot{\mathbf{q}}$, where $\mathbf{M}$ and $\mathbf{K}$ are the mass and stiffness matrices and $c_1$ and $c_2$ are constants of proportionality. Moreover, faster movements require a smaller integration time-step and a larger element number. System properties like flow rate and actuator free volume should also be taken into account. In such scenarios, the actuation pressure becomes a function of time, flow

rate, and actuator free volume. This function could be obtained by the system identification method or the derivation of the ideal gas equation.

## 5. Conclusions

In this paper, we present an ANCF-based dynamic model for soft actuators and validate this model by experiments. The ANCF approach is employed to represent variable curvature configurations of soft actuators. Based on this parameterization method, generalized forces are calculated and the dynamic model is derived by the principle of virtual work. With identified parameters, the Newmark method is utilized to solve the developed dynamic model and achieve real-time simulation. The prediction accuracy pf the dynamic model is experimentally validated. Under actuation pressure with frequencies of 0.4 Hz, 0.7 Hz, and 1.0 Hz, the dynamic model achieves substantial simulation error reductions of 37.91%, 46.31%, and 55.36% compared to the static ANCF-based model. The simulation error at the tip remains below 2.5% of the soft actuator's length when the sweep frequency actuation pressure is applied. With varying tip loads complex actuation pressure, the maximum simulation error remains below 2% of the soft actuator's length. We believe this research can pave the way for developing dynamic controllers for soft actuators, enhancing their wider applications in various fields.

Future work of the dynamic model attempts to improve simulation accuracy by incorporating additional effects such as nonlinear elastic forces, material viscosity, and fluid dynamics. We also plan to further establish dynamic models for multiple-segment soft continuum robots. Moreover, the proposed model will also be investigated to predict the risk of bursting and enhance the selection of soft actuators with a reduced probability of bursting.

## Data availability statement

All data that support the findings of this study are included within the article (and any supplementary files).

## Acknowledgments

This work was partially supported by the National Natural Science Foundation of China (Grant Nos. 52025057 and T2293725), the Science and Technology Commission of Shanghai Municipality (Grant No. 22511101700) and the State Key Laboratory of Mechanical System and Vibration (Grant No.MSVZD202301).

## ORCID iDs

Yu Rong https://orcid.org/0000-0003-1266-1562
Guoying Gu https://orcid.org/0000-0002-7778-4523

## References

[1] Rus D and Michael T T 2015 Design, fabrication and control of soft robots *Nature* **521** 467–75
[2] Yasa O, Toshimitsu Y, Michelis M Y, Jones L S, Filippi M, Buchner T and Katzschmann R K 2023 An overview of soft robotics *Annu. Rev. Control Robot. Auton. Syst.* **6** 1–29
[3] El-Atab N, Mishra R B, Al-Modaf F, Joharji L, Alsharif A A, Alamoudi H, Diaz M, Qaiser N and Mustafa Hussain M 2020 Soft actuators for soft robotic applications: a review *Adv. Intell. Syst.* **2** 2000128
[4] Wang Z, Kanegae R and Hirai S 2021 Circular shell gripper for handling food products *Soft Robot.* **8** 542–54
[5] Xie Z *et al* 2023 Octopus-inspired sensorized soft arm for environmental interaction *Sci. Robot.* **8** eadh7852
[6] Zhu J, Lyu L, Xu Y, Liang H, Zhang X, Ding H and Zhigang W 2021 Intelligent soft surgical robots for next-generation minimally invasive surgery *Adv. Intell. Syst.* **3** 2100011
[7] Feng M, Yang D and Guoying G 2021 High-force fabric-based pneumatic actuators with asymmetric chambers and interference-reinforced structure for soft wearable assistive gloves *IEEE Robot. Autom. Lett.* **6** 3105–11
[8] Tang Y, Chi Y, Sun J, Huang T-H, Maghsoudi O H, Spence A, Zhao J, Hao S and Yin J 2020 Leveraging elastic instabilities for amplified performance: Spine-inspired high-speed and high-force soft robots *Sci. Adv.* **6** eaaz6912
[9] Xavier M S, Fleming A J and Yong Y K 2021 Finite element modeling of soft fluidic actuators: Overview and recent developments *Adv. Intell. Syst.* **3** 2000187
[10] Moseley P, Manuel Florez J, Arun Sonar H, Agarwal G, Curtin W and Paik J 2016 Modeling, design and development of soft pneumatic actuators with finite element method *Adv. Eng. Mater.* **18** 978–88
[11] Katzschmann R K, Thieffry M, Goury O, Kruszewski A, Guerra T-M, Duriez C and Rus D 2019 Dynamically closed-loop controlled soft robotic arm using a reduced order finite element model with state observer *2019 2nd IEEE Int. Conf. on Soft Robotics (RoboSoft)* pp 717–24
[12] Duriez C 2013 Control of elastic soft robots based on real-time finite element method *2013 IEEE Int. Conf. on Robotics and Automation* pp 3982–7
[13] Caasenbrood B J, Pogromsky A Y and Nijmeijer H 2024 Sorotoki: a matlab toolkit for design, modeling and control of soft robots *IEEE Access* **12** 17604–38
[14] Fang G, Matte C-D, Kwok T-H and Wang C C L 2018 Geometry-based direct simulation for multi-material soft robots *2018 IEEE Int. Conf. on Robotics and Automation (ICRA)* pp 4194–9
[15] Robert J W III and Bryan A J 2010 Design and kinematic modeling of constant curvature continuum robots: a review *Int. J. Robot. Res.* **29** 1661–83
[16] Katzschmann R K, Della Santina C, Toshimitsu Y, Bicchi A and Rus D 2019 Dynamic motion control of multi-segment soft robots using piecewise constant curvature matched with an augmented rigid body model *2019 2nd IEEE Int. Conf. on Soft Robotics (RoboSoft)* pp 454–61
[17] Wang D, Jiang C and Guoying G 2024 Modeling and design of lattice-reinforced pneumatic soft robots *IEEE Trans. Robot.* **40** 606–23
[18] Oliver-Butler K, Till J and Rucker C 2019 Continuum robot stiffness under external loads and prescribed tendon displacements *IEEE Trans. Robot.* **35** 403–19
[19] Meier C, Popp A and Wall W A 2019 Geometrically exact finite element formulations for slender beams: Kirchhoff–love theory versus simo–reissner theory *Arch. Computat. Methods Eng.* **26** 163–243
[20] Till J, Aloi V, Riojas K E, Anderson P L, Webster III R J and Rucker C 2020 A dynamic model for concentric tube robots *IEEE Trans. Robot.* **36** 1704–18

[21] Villaggio P 1997 *Mathematical Models for Elastic Structures* (Cambridge University Press)
[22] Teejo Mathew A, Ben Hmida I, Armanini C, Boyer F and Renda F 2023 Sorosim: a matlab toolbox for hybrid rigid-soft robots based on the geometric variable-strain approach *IEEE Robot. Automat. Mag.* **30** 106–22
[23] Renda F, Boyer F'eric, Dias J and Seneviratne L 2018 Discrete cosserat approach for multisection soft manipulator dynamics *IEEE Trans. Robot.* **34** 1518–33
[24] Haihong Li, Xun L and Zheng G 2023 Piecewise linear strain cosserat model for soft slender manipulator *IEEE Trans. Robot.* **39** 2342–59
[25] Xu Q and Liu J 2023 Dynamic research on nonlinear locomotion of inchworm-inspired soft crawling robot *Soft Robot.* **10** 660–72
[26] Mastura Mustaza S, Elsayed Y, Lekakou C, Saaj C and Fras J 2019 Dynamic modeling of fiber-reinforced soft manipulator: a visco-hyperelastic material-based continuum mechanics approach *Soft Robot.* **6** 305–17
[27] Ishigaki T, Ayusawa K and Yamamoto K 2024 Comprehensive gradient computation framework of pcs model for soft robot simulation *IEEE Robot. Autom. Lett.* **9** 5990–7
[28] Huang X, Zou J and Guoying G 2021 Kinematic modeling and control of variable curvature soft continuum robots *IEEE/ASME Trans. Mechatronics* **26** 3175–85
[29] Huang X, Zhu X and Guoying G 2022 Kinematic modeling and characterization of soft parallel robots *IEEE Trans. Robot.* **38** 3792–806
[30] Xu Q and Liu J 2020 Effective enhanced model for a large deformable soft pneumatic actuator *Acta Mech. Sin.* **36** 245–55
[31] Shabana A A and Eldeeb A E 2021 Motion and shape control of soft robots and materials *Nonlinear Dyn.* **104** 165–89
[32] Gerstmayr J and Shabana A A 2006 Analysis of thin beams and cables using the absolute nodal co-ordinate formulation *Nonlinear Dyn.* **45** 109–30
[33] Sheng F, Zhong Z and Wang K-H 2020 Theory and model implementation for analyzing line structures subject to dynamic motions of large deformation and elongation using the absolute nodal coordinate formulation (ancf) approach *Nonlinear Dyn.* **101** 333–59
[34] Connolly F, Walsh C J and Bertoldi K 2017 Automatic design of fiber-reinforced soft actuators for trajectory matching *Proc. Natl Acad. Sci.* 114 51–56
[35] Berzeri M and Shabana A A 2000 Development of simple models for the elastic forces in the absolute nodal co-ordinate formulation *J. Sound Vib.* **235** 539–65
[36] Till J, Aloi V and Rucker C 2019 Real-time dynamics of soft and continuum robots based on cosserat rod models *Int. J. Robot. Res.* **38** 723–46
[37] Ahmed A S 2010 General method for modeling slope discontinuities and t-sections using ancf gradient deficient finite elements *J. Comput. Nonlinear Dyn.* **6** 024502
[38] Qiping X, Liu J and Lizheng Q 2019 Dynamic modeling for silicone beams using higher-order ancf beam elements and experiment investigation *Multibody Syst. Dyn.* **46** 307–28
[39] Courant R, Friedrichs K and Lewy H 1967 On the partial difference equations of mathematical physics *IBM J. Res. Dev.* **11** 215–34
[40] Hussein B, Negrut D and Shabana A A 2008 Implicit and explicit integration in the solution of the absolute nodal coordinate differential/algebraic equations *Nonlinear Dyn.* **54** 283–96
[41] Bonet J and Wood R D 1997 *Nonlinear Continuum Mechanics for Finite Element Analysis* (Cambridge University Press)